Dalton Transactions

ROYAL SOCIETY OF CHEMISTRY

PAPER

View Article Online
View Journal | View Issue

Cite this: *Dalton Trans.*, 2026, **55**, 2845

Room-temperature and one-minute synthesis of alcohol-soluble and ultra-small Eu-doped $CaMoO_4$ nanoparticles

Ling Zhong,[a] Mengxin Liu,*[b] Xin Su,[a] Chunyi Li,[a] Xinan Shi *[a] and Daocheng Pan *[a,b]

Received 18th December 2025,
Accepted 13th January 2026

DOI: 10.1039/d5dt03028e

rsc.li/dalton

Lanthanide (Ln^{3+}) doped alkaline earth metal molybdates ($AMoO_4$, A = Ca, Sr, Mg) have been widely investigated owing to their excellent photoluminescence properties. Alcohol-soluble and ultra-small Eu^{3+}-doped $CaMoO_4$ nanocrystals are prepared at room temperature within one minute using a propionic acid/propylamine-assisted method. Short-chain propionic acid and propylamine are employed as the capping agents, which is crucial for alcohol-soluble ability, controlling particle size and passivating surface defects. X-ray diffraction and transmission electron microscopy characterization revealed that the Eu^{3+}-doped $CaMoO_4$ nanoparticles have a pure tetragonal scheelite structure and an average particle size of 3.4 nm. Under UV light or high-energy X-ray excitation, Eu^{3+}-doped $CaMoO_4$ nanocrystals exhibit the intense characteristic emission of Eu^{3+} ions, which show a great potential application in high-quality displays, bio-imaging, and radiation detection.

Introduction

Rare earth ion doped alkaline earth metal molybdates ($AMoO_4$, A = Ca, Sr, Mg) have attracted extensive research interest due to their outstanding photoluminescence properties, rendering them promising candidates for a variety of applications such as high-quality display devices,[1,2] light-emitting diodes (LEDs),[3–6] scintillators,[7] and solar cells.[8,9] Among trivalent lanthanide ions (Ln^{3+}), the narrow emission bands originating from 4f–4f transitions make them ideal activators in luminescent materials.[10] Calcium molybdate ($CaMoO_4$), as an important member of the metal molybdate family, exhibits excellent physicochemical stability and serves as an efficient host lattice for luminescence.[11] Notably, $CaMoO_4$ itself shows intrinsic luminescence, where energy transfer from the host to dopant ions can yield blue to green emission under UV excitation.[11,12]

Conventional synthesis of Ln^{3+}-doped $CaMoO_4$ often relies on high-temperature solid-state reactions,[13,14] which not only consume significant energy but also introduce undesirable oxygen vacancies, thereby adversely affecting the luminescence performance. In recent years, several wet-chemical approaches, such as co-precipitation,[15,16] sol–gel processing,[17,18] and hydrothermal methods,[19–21] have been developed to prepare Ln^{3+}-doped $CaMoO_4$ nanocrystals. However, the luminescence efficiency of such nanocrystals remains considerably lower than that of their bulk counterparts sintered at high temperature,[13,14] highlighting the need for a synthetic strategy that combines high crystallinity, strong luminescence, and avoidance of high-temperature thermal treatment.

Our group has recently developed a room-temperature and short-chain ligand-assisted co-precipitation synthetic method for producing highly crystalline and strongly luminescent Ln^{3+}-doped nanocrystals, including Eu^{3+}-doped YVO_4,[22] Eu^{3+}-doped $CaMoO_4$,[23] Ce/Tb-codoped $NaYF_4$,[24] and Yb^{3+}/Nd^{3+}-doped $CaMoO_4$ nanocrystals.[25] These nanomaterials could be readily dispersed in chloroform for further solution processing. Nevertheless, the use of chloroform poses health and environmental concerns due to its toxicity. To address this issue, we report here a propionic acid/propylamine-assisted approach that enables rapid and room-temperature synthesis of alcohol-soluble Eu^{3+}-doped $CaMoO_4$ nanocrystals. The short-chain propionic acid and propylamine act as effective capping ligands, conferring ethanol solubility, controlling particle size and passivating surface defects. As a result, we have successfully obtained highly luminescent, alcohol-soluble Eu^{3+}-doped $CaMoO_4$ nanocrystals with a maximum photoluminescence quantum yield (PLQY) of 46.12%, demonstrating their potential for practical applications in eco-friendly optoelectronic devices.

[a]*Guangxi Key Laboratory of Advanced Rare Earth Materials, MOE Key Laboratory of New Processing Technology for Nonferrous Metals and Materials; School of Resources, Environment and Materials, Guangxi University, Nanning 530004, China. E-mail: xashi@gxu.edu.cn, dcpan@gxu.edu.cn*
[b]*School of Chemistry and Chemical Engineering, Guangxi University, Nanning 530004, China. E-mail: mxliu@st.gxu.edu.cn*

Experimental section

Chemicals

Ammonium molybdate ($(NH_4)_6Mo_7O_{24}$, 99%) was purchased from Beijing Chemical Works. Calcium nitrate ($Ca(NO_3)_2{\cdot}4H_2O$, A.R.), europium nitrate ($Eu(NO_3)_3{\cdot}6H_2O$, 99.99%), propionic acid (CH_3CH_2COOH, 99%), propylamine ($CH_3(CH_2)_2NH_2$, 99%), ethanol (CH_3CH_2OH, A.R.), and methanol (CH_3OH) were purchased from Aladdin Inc. All the chemicals are original without any purification.

Synthesis of Eu^{3+}-doped $CaMoO_4$ nanocrystals

First, 1.0 mL of propionic acid, 1.0 mL of propylamine, 1.0 mmol of $Ca(NO_3)_2{\cdot}4H_2O$ and $Eu(NO_3)_3{\cdot}6H_2O$ (x = Eu/(Eu + Ca), $0 \le x \le 0.25$), and 10.0 mL ethanol were mixed in a glass beaker (referred to as Solution A). Ammonium molybdate (1.0 mmol of MoO_4^{2-}) was dissolved in a mixed solution containing 4.0 mL of methanol and 1.0 mL of propylamine under sonication, forming Solution B. Solution A and Solution B were mixed and reacted under magnetic stirring at room temperature for 1 min to form a $Ca_{1-x}MoO_4{:}Eu_x^{3+}$ nanoparticle solution. An appropriate amount of acetonitrile was added to the precipitate and a white solid was obtained after centrifugation. Finally, $Ca_{1-x}MoO_4{:}Eu_x^{3+}$ nanocrystals were dispersed in ethanol after washing with acetonitrile.

Characterization

The $Ca_{1-x}MoO_4{:}x$Eu nanocrystals were characterized by XRD (Bruker D8 Discover) in the 2θ range from 10° to 70° with a scanning rate of 0.02° s^{-1}. Electron microscopy images were obtained using a transmission electron microscope (FEI TECNAIG2 F30). The chemical composition was determined using a Hitachi S-3400N scanning electron microscope equipped with an energy dispersive X-ray spectroscopy system. The chemical valence states were determined using X-ray photoelectron spectroscopy (XPS, Thermo Fisher ESCALAB 250Xi). Excitation and photoluminescence (PL) spectra, PL quantum yields (PLQYs), and PL lifetimes were measured using a Horiba Fluoromax-4 spectrometer and an Edinburgh FLS-1000 fluorescence spectrometer. Radioluminescence (RL) spectra were recorded using the Edinburgh FLS-1000 fluorescence spectrometer equipped with an X-ray tube (Tungsten target, Moxtek). The commercial LuAG:Ce crystal was employed to compare the light yields of the samples. The UV-vis diffuse reflectance spectrum was recorded using a UV-vis-near infrared spectrophotometer (Shimadzu, UV-3600 Plus). The Fourier transform infrared (FT-IR) spectrum was acquired using a Bruker Vertex 70 FT-IR spectrophotometer. The *I–V–L* curve of light emitting diodes was recorded using a Minolta LS-150 luminance meter and Keithley 2400.

Results and discussion

Recently, hydrophobic Eu^{3+}-doped $CaMoO_4$ nanocrystals were synthesized by a ligand-assisted co-precipitation method.[23] In this work, the alcohol-soluble Eu^{3+} doped $CaMoO_4$ nanocrystals were rapidly synthesized at room temperature within one minute, employing short-chain propionic acid and propylamine as capping ligands. It has been reported that the conversion rate from $Mo_7O_{24}^{6-}$ to MoO_4^{2-} is pH-dependent and accelerates under high pH conditions.[26] The addition of propylamine facilitates this transformation. The resulting MoO_4^{2-} precursor solution was then rapidly introduced into the Ca^{2+} solution, thereby inducing the instant nucleation and crystallization of $CaMoO_4$ nanoparticles. The entire reaction process can be completed within 5 seconds (see Fig. S1, SI). The acid–base reaction between propionic acid and propylamine generates acid–base ion pairs ($CH_3CH_2COO^-H_3N^+CH_2CH_2CH_3$), which function as capping ligands. This ligand system not only enables the nanocrystals to be highly dispersed in ethanol but also effectively controls particle size and passivates surface defects.[24] Purification was achieved by adding acetonitrile as an anti-solvent, followed by centrifugation. The successful coordination of propionic acid and propylamine on the surface of the Eu^{3+} doped $CaMoO_4$ nanocrystals was confirmed by FT-IR spectroscopy (Fig. 1). The characteristic absorption peaks observed for the C=O stretch from the carboxylate group and the N–H stretches from the amine group provide direct evidence of the presence of both capping agents.

The crystal structure of $CaMoO_4$, illustrated in Fig. 2a, features a scheelite-type tetragonal framework composed of MoO_4 tetrahedra and CaO_8 polyhedral units. Each MoO_4 tetrahedron shares its corners with four adjacent CaO_8 polyhedra *via* oxygen bridges.[27] Fig. 2b displays a series of X-ray diffraction (XRD) patterns of pristine $CaMoO_4$ and $Ca_{1-x}MoO_4{:}Eu_x^{3+}$ nanocrystals (x = 0.01–0.4). All diffraction peaks can be accurately indexed to the pure tetragonal scheelite structure of $CaMoO_4$ (JCPDS No. 07-0212), confirming the phase purity of the as-synthesized samples. No impurity-related peaks are detected. We found a systematic shift of the diffraction peaks

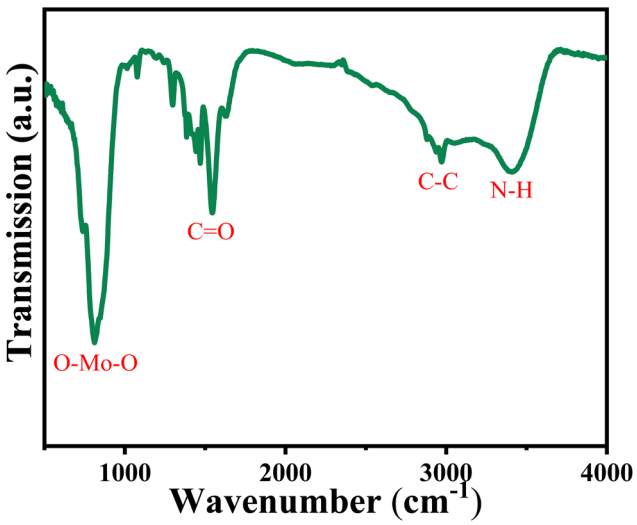

Fig. 1 FT-IR spectrum of propionic acid/propylamine-capped $Ca_{0.85}MoO_4{:}Eu_{0.15}^{3+}$ nanocrystals.

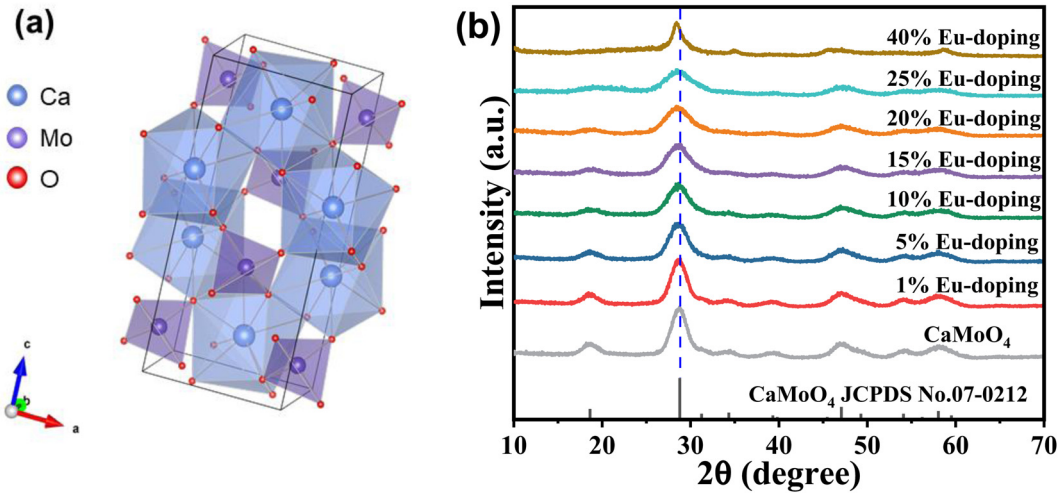

Fig. 2 (a) Polyhedral representation of a $CaMoO_4$ unit cell. (b) Powder X-ray diffraction (XRD) of $Ca_{1-x}MoO_4:Eu_x^{3+}$ (x = 0.01, 0.05, 0.1, 0.15, 0.2, 0.25, and 0.4) nanocrystals with different Eu doping concentrations.

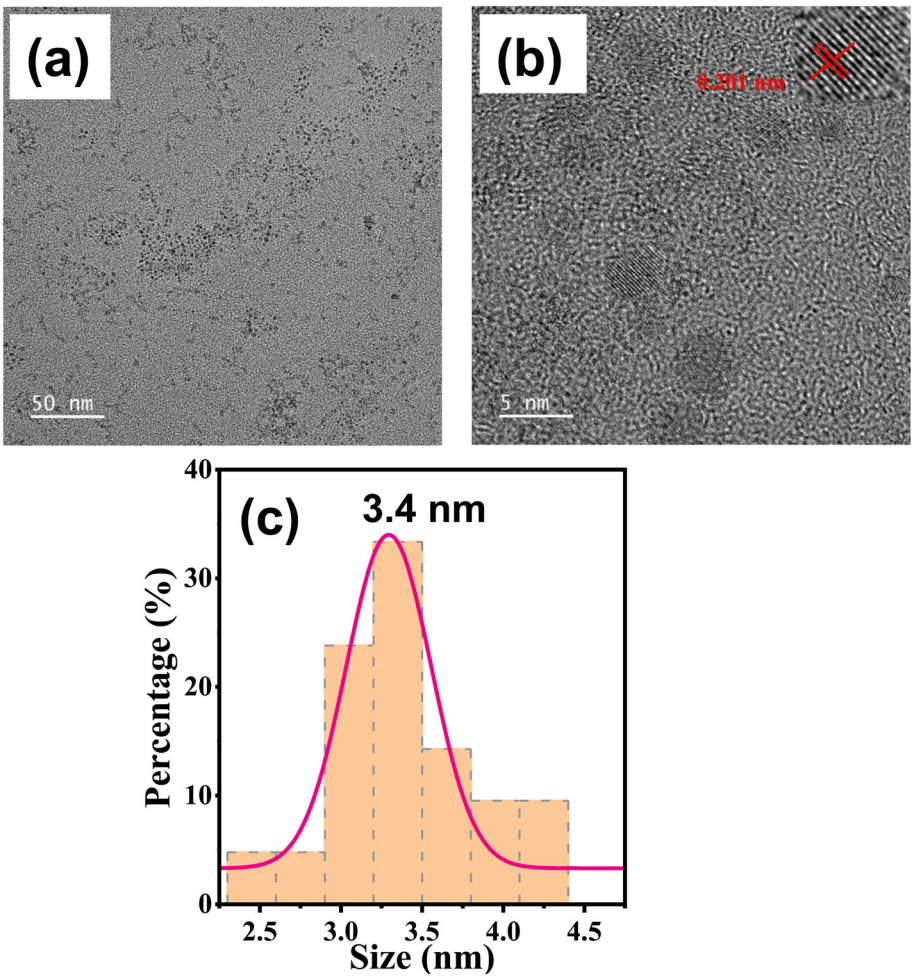

Fig. 3 (a) TEM and (b) HR-TEM images of $Ca_{0.85}MoO_4:Eu_{0.15}^{3+}$ nanocrystals and (c) the size distribution of $Ca_{0.85}MoO_4:Eu_{0.15}^{3+}$ nanocrystals.

toward lower 2θ angles with increasing Eu^{3+} concentration, as notably exemplified by the peak around 28.8°. This shift indicates an expansion of the unit cell volume – a phenomenon that appears counterintuitive given the smaller ionic radius of Eu^{3+} ions (1.066 Å) compared to that of Ca^{2+} ions (1.12 Å). However, such anomalous peak shifting has been documented in previous studies.[28–30] The substitution of Ca^{2+} by Eu^{3+} introduces a difference in electronegativity (1.132 for Ca^{2+} *vs.* 1.377 for Eu^{3+}).[31] The higher electronegativity of Eu^{3+} draws oxygen ions away from the central Mo^{6+} cation, leading to an expansion of the MoO_4 tetrahedra. This local structural distortion subsequently propagates, resulting in an overall increase in the unit cell volume.[28]

The morphology and microstructure of the as-synthesized Eu^{3+}-doped $CaMoO_4$ nanocrystals were examined by transmission electron microscopy (TEM). As shown in Fig. 3a, the nanocrystals are uniformly distributed and well-dispersed. A corresponding high-resolution TEM (HR-TTEM) image (Fig. 3b) reveals clear lattice fringes with an interplanar spacing of 0.201 nm, which matches the (204) crystallographic planes of the tetragonal $CaMoO_4$ structure. Furthermore, statistical analysis of the particle size distribution (Fig. 3c) indicates an average nanocrystal diameter of 3.4 nm and a narrow size distribution.

Since Eu^{3+}-doped $CaMoO_4$ nanocrystals are capped by propionic acid and propylamine, they are highly soluble in ethanol, forming a transparent and homogeneous colloidal solution. Fig. 4a and b display the excitation and emission spectra of $Ca_{0.85}MoO_4:Eu_{0.15}^{3+}$ nanocrystal powder and nanocrystal solution prepared at room temperature. In the excitation spectrum of the $Ca_{0.85}MoO_4:Eu_{0.15}^{3+}$ nanocrystal powder, a broad band ranging from 240 to 350 nm with a maximum at 280 nm is observed, which is ascribed to the charge transfer (CT) transitions of $O^{2-} \rightarrow Mo^{6+}$ and $O^{2-} \rightarrow Eu^{3+}$ groups.[12] Several weaker and sharper peaks are also present at 362 nm ($^7F_0 \rightarrow {}^5D_4$), 382 nm ($^7F_0 \rightarrow {}^5L_7$), 395 nm ($^7F_0 \rightarrow {}^5L_6$), 416 nm ($^7F_0 \rightarrow {}^5D_3$), and 465 nm ($^7F_0 \rightarrow {}^5D_2$), corresponding to the characteristic 4f–4f transitions of Eu^{3+} ions.[31,32] Compared to the powder sample, the excitation spectrum of the solution sample exhibits a slight red shift in the CT band (260–350 nm, centered at 300 nm), along with a series of weaker 4f–4f transition peaks in the 350–500 nm region. This behavior can be attributed to the dispersed state of the nanocrystals in ethanol, as opposed to the aggregated powder form.[23] The ultrasmall size of the nanocrystals also results in reduced light scattering in solution. Furthermore, the isolation of individual nanocrystals in the solution leads to a lower density of luminescent centers per unit volume and a decrease in energy transfer efficiency. As shown in Fig. 4a and b, the characteristic emission lines of Eu^{3+} corresponding to the $^5D_0 \rightarrow {}^7F_J$ (J = 1–4) transitions are clearly observed. The most intense peak at 615 nm is assigned to the $^5D_0 \rightarrow {}^7F_2$ electric dipole transition, which is highly sensitive to the local crystal field environment around the Eu^{3+} ions. Other emission

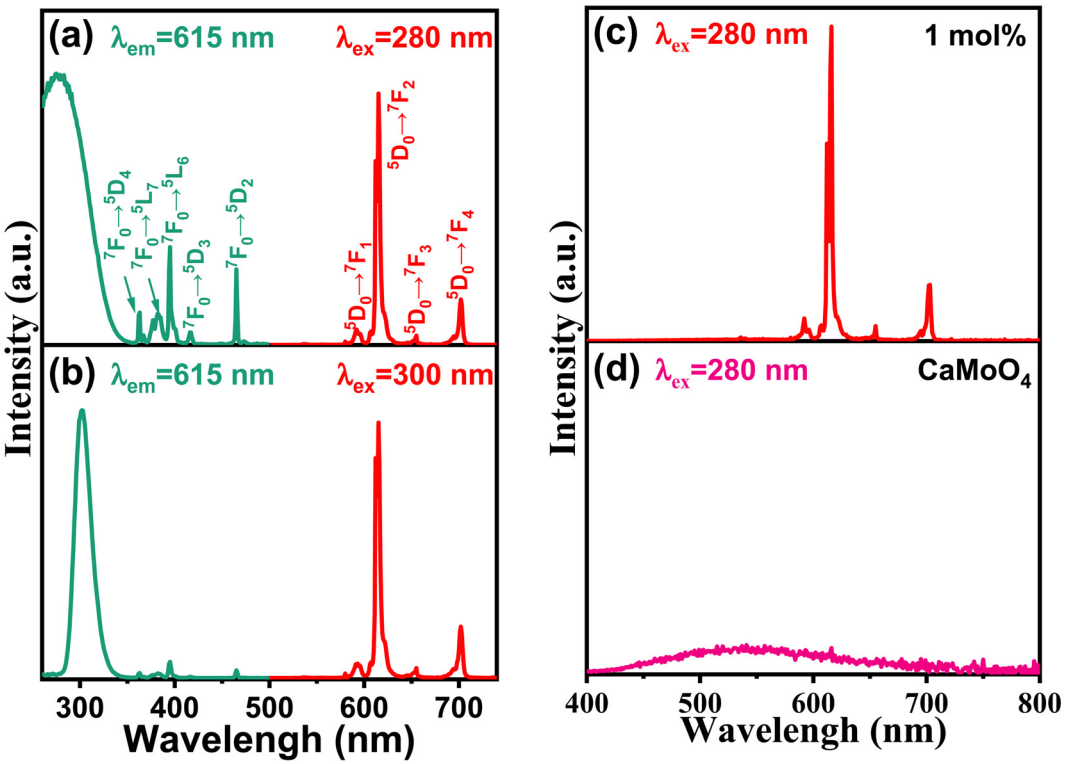

Fig. 4 Excitation and emission spectra of (a) the $Ca_{0.85}MoO_4:Eu_{0.15}^{3+}$ nanocrystal powder and (b) $Ca_{0.85}MoO_4:Eu_{0.15}^{3+}$ solution in ethanol. PL spectra of (c) the $Ca_{0.99}MoO_4:Eu_{0.01}^{3+}$ nanocrystal powder and (d) pristine $CaMoO_4$ nanocrystal powder.

peaks at 592 nm ($^5D_0 \rightarrow {}^7F_1$), 652 nm ($^5D_0 \rightarrow {}^7F_3$), and 700 nm ($^5D_0 \rightarrow {}^7F_4$) are attributed to magnetic dipole transitions. The dominance of the $^5D_0 \rightarrow {}^7F_2$ transition over the $^5D_0 \rightarrow {}^7F_1$ transition in both powder and solution samples indicates that the Eu^{3+} ions occupy low-symmetry sites lacking an inversion center.[33] This can be quantitatively confirmed by the asymmetry ratio, $R = I(^5D_0 \rightarrow {}^7F_2)/I(^5D_0 \rightarrow {}^7F_1)$, which is widely used to probe the local environment of Eu^{3+} ions.[34,35] The calculated R values of 16.7 for the powder and 18.2 for the solution support the incorporation of Eu^{3+} ions into low-symmetry sites, further demonstrating that Ca^{2+} ions on the surface and inner region of $CaMoO_4$ nanocrystals can be replaced by Eu^{3+} ions. Fig. 4c and d compare the photoluminescence intensities of 1.0 mol% Eu^{3+}-doped $CaMoO_4$ nanocrystals and undoped $CaMoO_4$ nanocrystals under 280 nm excitation. The intrinsic emission from the MoO_4^{2-} groups is significantly weaker than the Eu^{3+}-related emission, indicating the efficient energy transfer from the MoO_4^{2-} host to the Eu^{3+} ions, even at low doping levels (1.0 mol%).[36] This efficient energy transfer also confirms the successful incorporation of Eu^{3+} into the $CaMoO_4$ lattice, in agreement with the XRD analysis.

In addition, the UV-vis diffuse reflectance spectrum of $Ca_{0.85}MoO_4:Eu_{0.15}^{3+}$ nanocrystals is shown in Fig. 5a, revealing strong optical absorption in the 200–350 nm range. The Tauc plot method was used to estimate the optical band gap energy (E_g) from the absorption data,[37] yielding a band gap value of 3.79 eV (Fig. 5b). The obtained E_g is approximately 0.38 eV larger than previously reported theoretical values,[38] which can be reasonably attributed to the quantum size effect in the ultrasmall nanocrystals.[39] To investigate the influence of Eu^{3+} doping concentration on the PL intensity, a series of $Ca_{1-x}MoO_4:Eu_x^{3+}$ nanocrystals with varying x values were synthesized. The photoluminescence quantum yield (PLQY) of each sample was measured under 280 nm excitation, as summarized in Fig. 5c. It was found that the PLQY initially increases with rising Eu^{3+} concentration, reaching a maximum value of 46.12% at x = 0.15 (15 mol%). Beyond this optimal doping level, the PLQY gradually decreases, though it remains

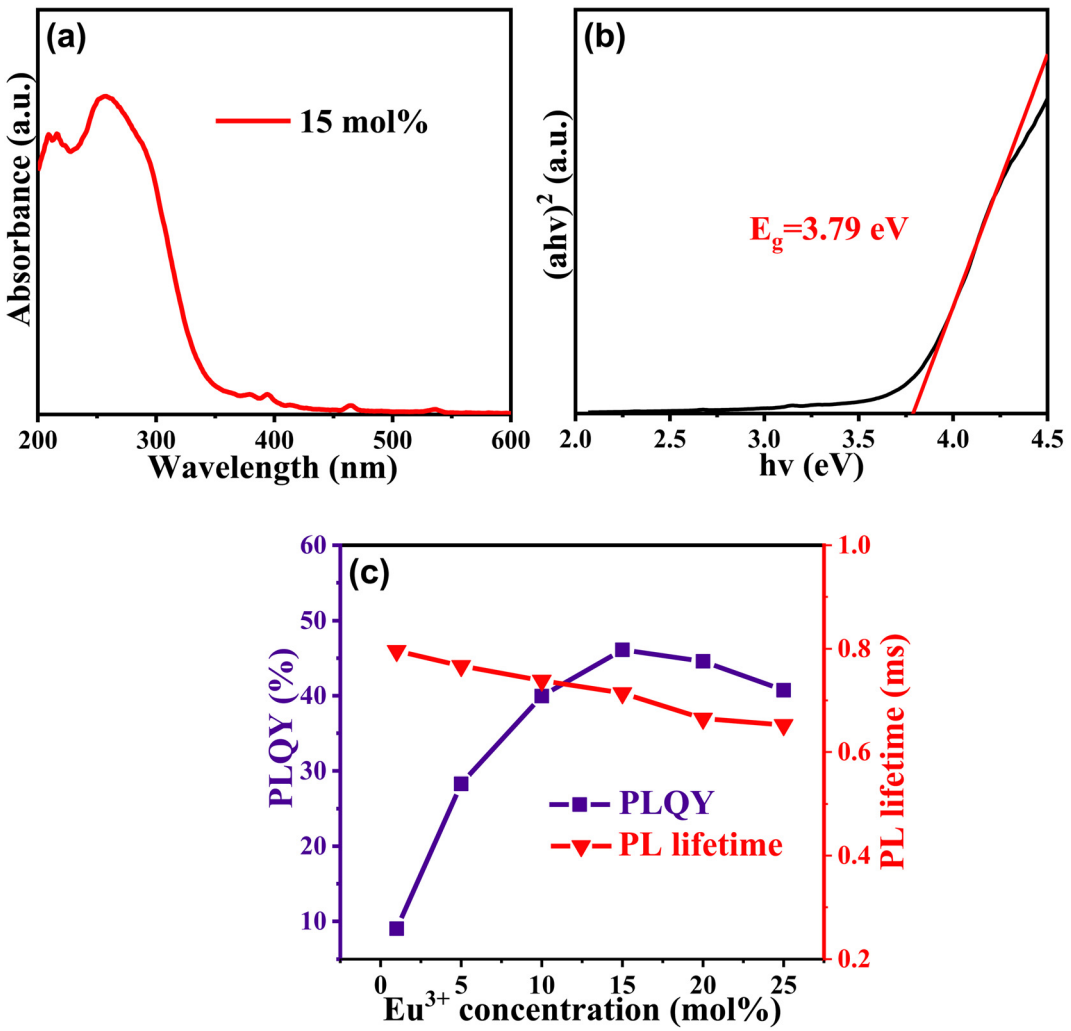

Fig. 5 (a) UV-vis diffuse reflectance spectrum and (b) the optical band gap of $Ca_{0.85}MoO_4:Eu_{0.15}^{3+}$ nanocrystals. (c) PLQYs and PL lifetimes of $Ca_{1-x}MoO_4:Eu_x^{3+}$ nanocrystals.

above 40% even at $x = 0.25$. This phenomenon results from the concentration quenching effect.[40,41] To eliminate measurement uncertainty, three different batch tests were conducted on the PLQYs of Eu^{3+}-doped $CaMoO_4$ nanocrystals (Table S1, SI). At lower concentrations, increasing dopant density enhances the energy transfer efficiency from the $CaMoO_4$ host to Eu^{3+} ions. However, beyond a critical threshold, the average distance between Eu^{3+} ions becomes sufficiently small to promote non-radiative energy migration among them, leading to a reduction in overall emission efficiency.[12] Additionally, the presence of propionic acid and propylamine capping ligands may help mitigate interparticle energy transfer by isolating individual nanocrystals, thereby partially alleviating the concentration quenching effect.[23] The comparisons between alcohol-soluble Eu^{3+}-doped $CaMoO_4$ nanocrystals and our previously reported hydrophobic nanocrystals are summarized in Table S2 (SI). It is evident that the capping agents have a vastly important influence on PLQY and solvent compatibility. Besides, the comparisons of PLQY and synthesis time with those of previously reported Eu-doped $CaMoO_4$ phosphors prepared with different synthetic methods are presented in Table S3 (SI).

The luminescence decay dynamics of $Ca_{1-x}MoO_4:Eu_x^{3+}$ nanocrystals were investigated by monitoring the $^5D_0 \rightarrow {}^7F_2$ transition at 615 nm under 280 nm excitation (Fig. 6). Consistent with previous reports,[11,12] all decay curves exhibit biexponential behavior, which were well fitted using the function:

$$I(t) = I_0 + A_1 e^{-\frac{x}{\tau_1}} + A_2 e^{-\frac{x}{\tau_2}}$$

where I(t) and I_0 represent the luminescence intensities at time t and 0, τ_1 and τ_2 are the decay time constants, and A_1 and A_2 denote their respective amplitudes. In luminescent materials, the decay kinetics are strongly influenced by the nature of luminescent centers, energy transfer processes, and defect-related interactions.[42,43] A biexponential decay profile often arises when Eu^{3+} ions occupy multiple distinct crystallographic sites within the host lattice, forming different luminescent centers. In the present case, Eu^{3+} ions are expected to substitute for Ca^{2+} ions in low-symmetry sites, which could support more than one type of local coordination environment. Additionally, the room-temperature synthesis used here is known to yield nanocrystals with relatively low oxygen vacancy concentrations,[23] thereby reducing the defect-related nonradiative decay. Therefore, the observed biexponential decay is likely attributable to energy transfer from the $CaMoO_4$ host to the Eu^{3+} activators and/or the presence of multiple luminescent centers.[36,43]

The average lifetime (τ_{av}) was calculated using the expression:

$$\tau_{av} = \frac{A_1\tau_1^2 + A_2\tau_2^2}{A_1\tau_1 + A_2\tau_2}$$

As summarized in Fig. 5c, the average lifetime of $Ca_{1-x}MoO_4:Eu_x^{3+}$ nanocrystals gradually decreases with

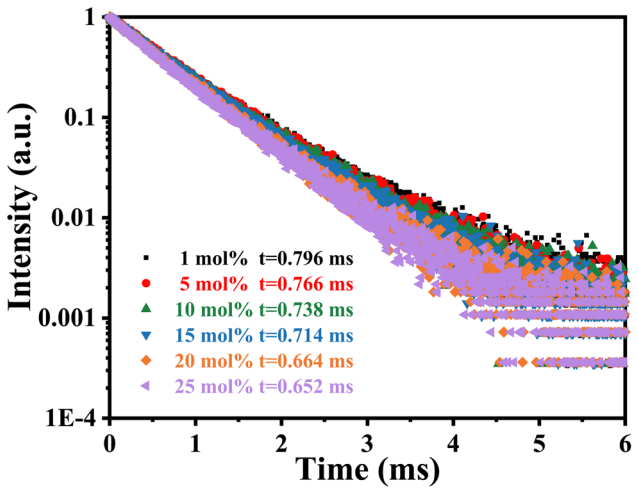

Fig. 6 PL decay curves of Eu^{3+}-doped $CaMoO_4$ nanocrystals with different Eu^{3+} doping concentrations.

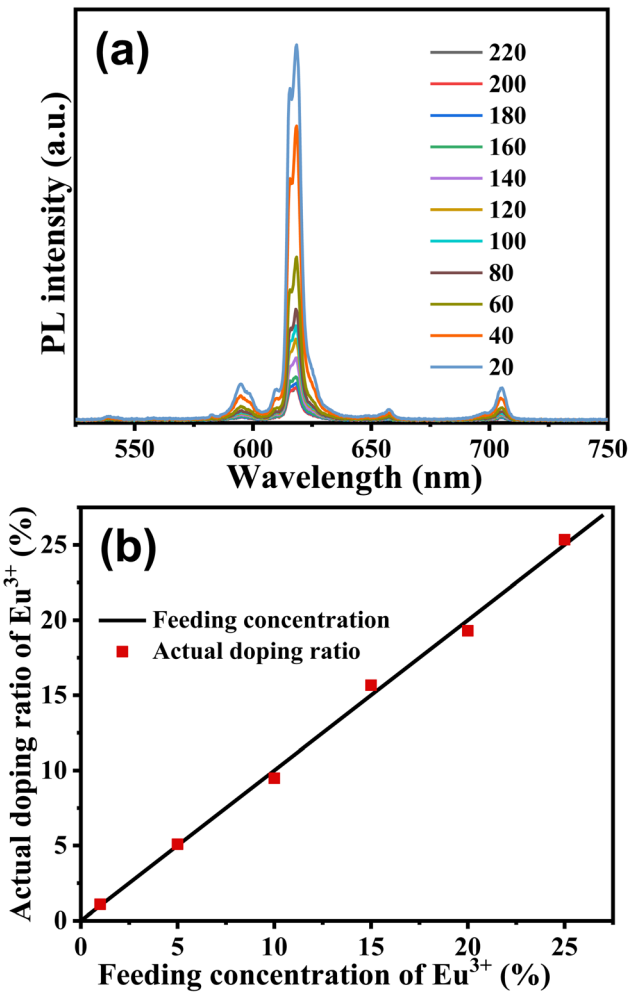

Fig. 7 (a) Temperature-dependent PL spectra of $Ca_{0.85}MoO_4:Eu_{0.15}^{3+}$ nanocrystals. (b) Plot of the actual doping ratio and feeding concentration of Eu^{3+} ions in $Ca_{1-x}MoO_4:Eu_x^{3+}$ nanocrystals detected by EDS.

increasing Eu^{3+} doping concentration. Specifically, τ_{av} declines from 0.796 ms to 0.652 ms as the doping level rises from 1 mol% to 25 mol%. This reduction in lifetime is a clear signature of concentration quenching, wherein higher dopant densities promote nonradiative energy migration among neighboring Eu^{3+} ions,[44] thereby shortening the observed luminescence decay time.

To evaluate the practical application potential of the luminescent nanocrystals, the thermal stability of $CaMoO_4:Eu^{3+}$ was systematically investigated. The temperature-dependent PL spectra of $Ca_{0.85}MoO_4:Eu_{0.15}^{3+}$ nanocrystals were measured over a temperature range of 20–200 °C. As shown in Fig. 7a, the position and shape of the emission profiles remain largely unchanged with increasing temperature. However, the PL intensity exhibits a significant decrease, demonstrating typical thermal quenching behavior.[45,46] This sensitive temperature-dependent luminescence suggests that the $Ca_{0.85}MoO_4:Eu_{0.15}^{3+}$ nanocrystals hold promise as an optical temperature-sensing material. The chemical compositions and actual Eu^{3+} doping concentration in $Ca_{1-x}MoO_4:Eu_x^{3+}$ nanocrystals were determined by energy-dispersive X-ray spectroscopy (EDS). From Fig. 7b, it can be seen that actual Eu^{3+} doping concentrations are close to the feeding concentration of Eu^{3+} ions.

The oxidation states of constituent elements in the 10 mol% Eu^{3+}-doped $CaMoO_4$ nanocrystals were analyzed by X-ray photoelectron spectroscopy (XPS), with the C 1s peak at 284.8 eV used as a reference. As shown in Fig. 8a, the Ca 2p spectrum exhibits two peaks at 347.1 eV ($2p_{3/2}$) and 350.8 eV ($2p_{1/2}$), consistent with the +2 oxidation state of calcium. The Mo 3d core-level spectrum (Fig. 8b) displays doublets at 232.7 eV ($3d_{5/2}$) and 235.7 eV ($3d_{3/2}$), confirming the +6 oxidation state of molybdenum. Fig. 8c shows two XPS peaks of Eu 3d at 1134.3 eV for $3d_{5/2}$ and 1164.8 eV for $3d_{3/2}$, indicating the presence of Eu^{3+} ions. The O 1s spectrum (Fig. 8d) is asymmetric and can be deconvoluted into two components: the lower binding energy peak at 530.5 eV is assigned to lattice oxygen in $CaMoO_4$, while the higher binding energy peak at 532.4 eV is attributed to surface-adsorbed organic ligands.[12,47]

Additionally, the $Ca_{1-x}MoO_4:Eu_x^{3+}$ nanocrystals can also be excited by high-energy X-rays to produce luminescence. The proposed scintillation mechanism in Eu^{3+}-doped $CaMoO_4$ nanocrystals is illustrated in Fig. 9a.[48–50] Upon X-ray irradiation, high-energy photons interact with the nanocrystals *via* the photoelectric effect and Compton scattering, generating hot electrons and deep holes. These primary carriers subsequently produce a large number of secondary electrons through Auger processes and electron–electron scattering,

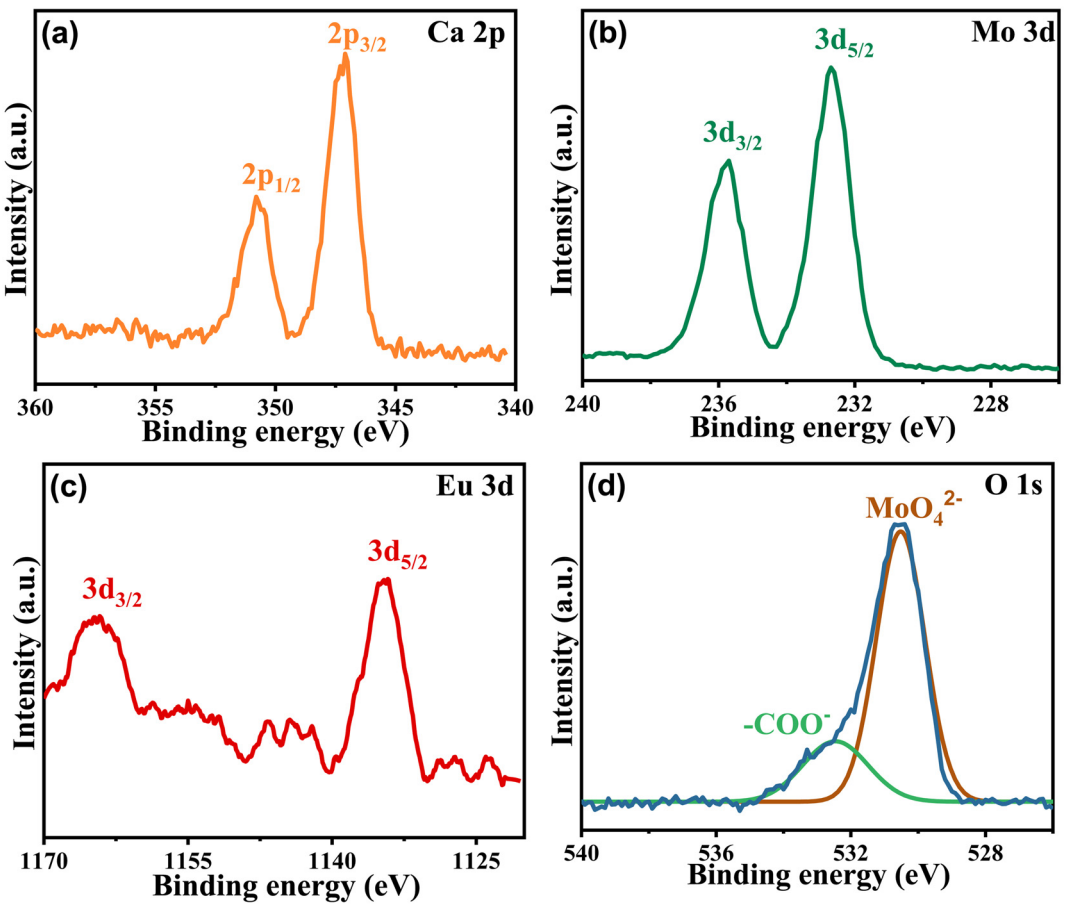

Fig. 8 XPS spectra of $Ca_{0.9}MoO_4:Eu_{0.1}^{3+}$ nanocrystals; (a) Ca 2p; (b) Mo 3d; (c) Eu 3d; and (d) O 1s.

resulting in numerous electron–hole pairs with lower kinetic energy. These charge carriers then migrate through the lattice and eventually transfer their energy to Eu^{3+} ions, exciting them and leading to characteristic visible emission. Fig. 9b shows the radioluminescence (RL) spectra of undoped and Eu^{3+} doped $CaMoO_4$ nanocrystals under X-ray excitation. The doped samples show the characteristic emission of Eu^{3+} ions and the peaks are labelled in the emission spectra. The $^5D_0 \rightarrow {}^7F_J$ (J = 1–4) transitions of Eu^{3+} ions provide sharp peaks at 592, 615, 654, and 702 nm. The RL intensity initially increases with Eu^{3+} concentration and reaches a maximum at 15 mol%, beyond which concentration quenching likely occurs. Therefore, the 15 mol% doped sample ($Ca_{0.85}MoO_4:Eu_{0.15}{}^{3+}$) was selected for further investigation. As shown in Fig. 9c, the RL intensity increases steadily with rising X-ray dose, and notably, the material shows detectable sensitivity even at a low dose rate of 0.38 μGy s^{-1}. Furthermore, a comparison of the RL intensity between the $Ca_{0.85}MoO_4:Eu_{0.15}{}^{3+}$ nanocrystals and a commercial LuAG:Ce scintillator is provided in Fig. 9d, demonstrating the promising potential of the developed Eu^{3+}-doped $CaMoO_4$ nanocrystals for scintillation applications. The RL spectra of both our sample and the reference LuAG:Ce scintillator were recorded separately but sequentially under an identical instrumental setup and X-ray excitation parameters. The integrated area in each respective RL spectrum was then calculated. The comparison of these integrated intensities forms the basis for assessing their relative RL efficiency. This method offers a straightforward and experimentally robust means for a head-to-head comparison. It is widely used in the field to quickly rank the performance of new scintillator materials against established benchmarks under equivalent conditions. However, this comparative approach has some limitations. First, the result indicates which material emits more light under the specific test conditions used but does not yield an absolute light yield value. Second, minor intensity fluctuations in the X-ray beam between the two sequential measurements could introduce a small degree of uncertainty into the direct intensity comparison.

This study focuses on the potential application of alcohol-soluble Eu^{3+}-doped $CaMoO_4$ luminescent nanocrystals, which form a transparent colloidal solution in ethanol. Using the propionic acid/propylamine-assisted method, $Ca_{0.85}MoO_4:Eu_{0.15}{}^{3+}$ nanocrystals were dispersed in ethanol with a concentration of 10 mg mL^{-1}. The transparent nanocrystal solution can remain stable in air for at least 24 hours (Fig. S2, SI). The uniform luminescent thin film can be deposited on a glass substrate *via* spin-coating (inset of Fig. 10a). Furthermore, a deep-UV LED chip was coated with the nanocrystal film; when

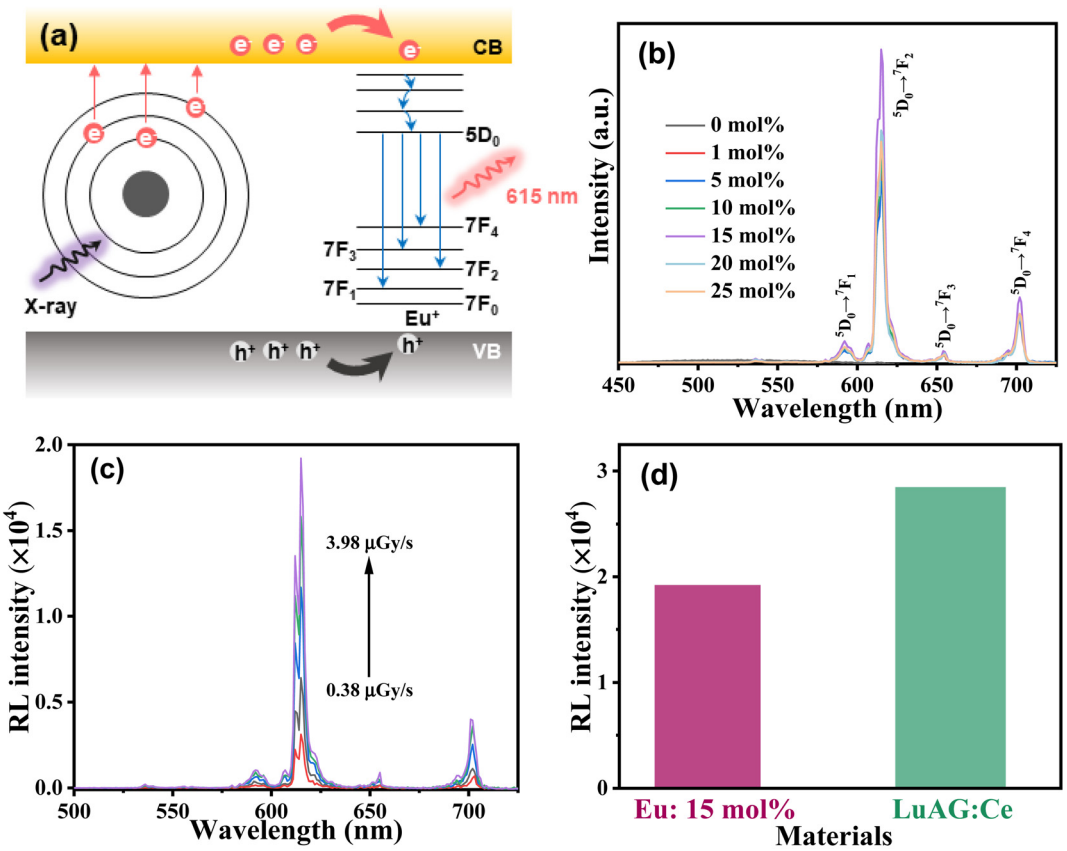

Fig. 9 (a) Radioluminescence (RL) mechanism of Eu^{3+}-doped $CaMoO_4$ nanocrystals. (b) RL spectra of the Eu^{3+}-doped $CaMoO_4$ nanocrystals with different Eu^{3+} doping concentrations. (c) RL spectra of the $Ca_{0.85}MoO_4:Eu_{0.15}{}^{3+}$ nanocrystals under different X-ray doses. (d) Comparison of the RL intensity between $Ca_{0.85}MoO_4:Eu_{0.15}{}^{3+}$ nanocrystals and commercial LuAG:Ce scintillator crystals.

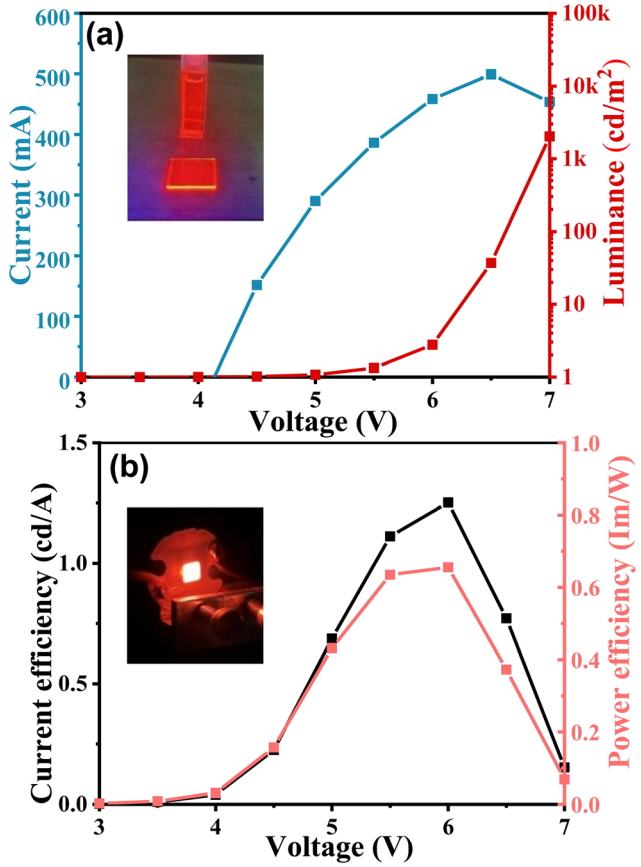

Fig. 10 (a) Current–voltage–luminance (*I–V–L*) curves of a red-emitting LED; inset: the picture of $Ca_{0.85}MoO_4:Eu_{0.15}^{3+}$ nanocrystal solution and thin film. (b) Current efficiency–voltage–power efficiency curves of the red-emitting LED, inset: the photograph of the red-emitting LED.

excited by 280 nm UV light, the LED can emit bright red light, as shown in the inset of Fig. 10b. Fig. 10a displays the current–voltage–luminance (*I–V–L*) characteristics of the resulting red-emitting LED. The device achieves a maximum luminance of 14 503 cd m^{-2}. In addition, Fig. 10b presents the current efficiency and power efficiency as functions of voltage. The LED exhibits a maximum current efficiency of 1.25 cd A^{-1} and a maximum power efficiency of 0.65 lm W^{-1}. These results demonstrate that the highly luminescent and alcohol-soluble Eu^{3+}-doped $CaMoO_4$ nanocrystals are promising candidates for use in high-quality display technologies.

Conclusions

In conclusion, we report a room-temperature synthetic route utilizing propionic acid/propylamine as co-ligands to rapidly produce alcohol-soluble Eu^{3+}-doped $CaMoO_4$ nanocrystals. This approach strikes a balance between speed, operational simplicity, and eco-friendliness. Notably, the lattice expansion observed at higher Eu^{3+} doping levels is explained by a local structural distortion mechanism driven by the higher electronegativity of Eu^{3+}. The obtained nanocrystals are ultrasmall (~3.4 nm) and highly efficient (PLQY = 46.12%), and exhibit scintillation properties comparable to those of LuAG:Ce. These findings reveal that our Eu^{3+}-doped $CaMoO_4$ nanocrystals are highly promising for advancing applications in high-quality displays and radiation detection.

Conflicts of interest

The authors declare no competing financial interest.

Data availability

Data provided in the article and the supplementary information (SI) are available on request from the corresponding author.

Supplementary information (SI): photographs of nanocrystal crude solutions at diffrent reaction times; detailed PLQY values; photographs of nanocrystal solution after different storage times. See DOI: https://doi.org/10.1039/d5dt03028e.

Acknowledgements

This work was supported by Guangxi Provincial Science and Technology Development Program (No. 2023GXNSFDA026056), Guangxi Science and Technology Major Project (No. ZY24212006 and No. AA23073018), and the Special Fund for Science and Technology Development of Guangxi (Grant No. AD25069078).

References

1 N. N. Munirajappa, R. B. Basavaraj, D. P. Aarti, M. B. M. Reddy, G. Nagaraju, H. M. S. Kumar, T. Chandrasekhar and A. S. Rathod, *J. Mol. Struct.*, 2025, **1319**, 139331.
2 J. Zhang, R. Li, L. Liu, L. Li, L. Zou, S. Gan and G. Ji, *Ultrason. Sonochem.*, 2014, **21**, 1736–1744.
3 M. H. Fang, J. L. Leaño and R. S. Liu, *ACS Energy Lett.*, 2018, **3**, 2573–2586.
4 A. Khanna and P. S. Dutta, *J. Solid State Chem.*, 2013, **198**, 93–100.
5 L. Y. Zhou, J. S. Wei, L. H. Yi, F. Z. Gong, J. L. Huang and W. Wang, *Mater. Res. Bull.*, 2009, **44**, 1411–1414.
6 X. A. Lin, X. S. Qiao and X. P. Fan, *Solid State Sci.*, 2011, **13**, 579–583.
7 X. Zhu, R. Zhou, Z. Wang, S. Thomas, P. Maity, L. Gutiérrez-Arzaluz, W. Wu, T. Sun, T. Jin, H. Cai, J.-X. Wang, H. N. Alshareef, O. M. Bakr, Y. Zhu and O. F. Mohammed, *ACS Energy Lett.*, 2024, **9**, 5137–5144.
8 A. Verma and S. K. Sharma, *Ceram. Int.*, 2017, **43**, 8879–8885.
9 A. R. D. Stigger, V. F. Hernandes, M. M. Ferrer and M. L. Moreira, *New J. Chem.*, 2023, **47**, 12458–12467.

10 S. Gai, C. Li, P. Yang and J. Lin, *Chem. Rev.*, 2013, **114**, 2343–2389.
11 C. R. R. Almeida, L. X. Lovisa, A. A. G. Santiago, M. S. Li, E. Longo, C. A. Paskocimas, F. V. Motta and M. R. D. Bomio, *J. Mater. Sci.: Mater. Electron.*, 2017, **28**, 16867–16879.
12 S. K. Gupta, M. Sahu, P. S. Ghosh, D. Tyagi, M. K. Saxena and R. M. Kadam, *Dalton Trans.*, 2015, **44**, 18957–18969.
13 P. Du and J. S. Yu, *Mater. Res. Bull.*, 2015, **70**, 553–558.
14 F. W. Kang, Y. H. Hu, H. Y. Wu, G. F. Ju, Z. F. Mu and N. N. Li, *J. Rare Earths*, 2011, **29**, 837–842.
15 J.-Y. Jung, *Materials*, 2022, **15**, 2078.
16 Y. B. Xiang, J. M. Song, G. Hu and Y. Liu, *Appl. Surf. Sci.*, 2015, **349**, 374–379.
17 G. Braziulis, R. Stankeviciute and A. Zalga, *Mater. Sci.*, 2014, **20**, 90–96.
18 Y. Y. Xu, X. M. Li, W. L. Li and W. J. Yang, *Optoelectron. Adv. Mater., Rapid Commun.*, 2016, **10**, 78–81.
19 N. C. Manh, L. T. H. Nguyen, T. M. Xuan, H. D. Tra, T. T. Anh Duong, L. T. T. Nguyen, H. Van Pham, M. N. Ha, V. H. Nguyen, H. D. Chau and T. K. Ngan Tran, *J. Lumin.*, 2023, **258**, 119776.
20 J. Bhagwan, S. K. Hussain and J. S. Yu, *ACS Sustainable Chem. Eng.*, 2019, **7**, 12340–12350.
21 X. F. Wang, G. H. Peng, N. Li, Z. H. Liang, X. Wang and J. L. Wu, *J. Alloys Compd.*, 2014, **599**, 102–107.
22 B. Li, M. Liu, X. Shi, Q. Cao, Z. Ni, C. Lu and D. Pan, *J. Phys. Chem. C*, 2023, **127**, 5075–5081.
23 M. Liu, X. Shi, Q. Cao, B. Li, Z. Ni, C. Lu, D. Pan and B. Zou, *Small*, 2023, **19**, 202301680.
24 J. Wei, M. Liu, X. Shi and D. Pan, *Inorg. Chem.*, 2024, **63**, 6408–6417.
25 M. Liu, J. Pan, X. Shi, B. Zou and D. Pan, *Laser Photonics Rev.*, 2025, **19**, 2401259.
26 W. S. Wang, Y. X. Hu, J. Goebl, Z. D. Lu, L. Zhen and Y. D. Yin, *J. Phys. Chem. C*, 2009, **113**, 16414–16423.
27 A. K. Parchur and R. S. Ningthoujam, *Dalton Trans.*, 2011, **40**, 7590–7594.
28 A. I. Becerro, M. Allix, M. Laguna, D. González-Mancebo, C. Genevois, A. Caballero, G. Lozano, N. O. Núñez and M. Ocaña, *J. Mater. Chem. C*, 2018, **6**, 12830–12840.
29 H. Wu, Y. Hu, W. Zhang, F. Kang, N. Li and G. Ju, *J. Sol-Gel Sci. Technol.*, 2012, **62**, 227–233.
30 C. Mazzariol, F. Tajoli, A. E. Sedykh, P. Dolcet, J.-D. Grunwaldt, K. Müller-Buschbaum and S. Gross, *ACS Appl. Nano Mater.*, 2023, **6**, 15510–15520.
31 R. Wangkhem, T. Yaba, N. S. Singh and R. S. Ningthoujam, *J. Appl. Phys.*, 2018, **123**, 124303.
32 M. N. Luwang, R. S. Ningthoujam, S. K. Srivastava and R. K. Vatsa, *J. Am. Chem. Soc.*, 2011, **133**, 2998–3004.
33 H. N. Van, M. T. Y. Thanh, V. H. Pham, P. V. Huan, V. T. N. Minh, P. A. Tuan and H. T. Duy, *Opt. Mater.*, 2022, **132**, 112831.
34 S. Wang, Y. Xu, T. Chen, W. Jiang, J. Liu, X. Zhang, W. Jiang and L. Wang, *J. Alloys Compd.*, 2019, **789**, 381–391.
35 P. Ostellari, F. Tajoli, I. Fortunati, T. Carofiglio, D. Badocco, P. Pastore and S. Gross, *CrystEngComm*, 2024, **26**, 6052–6064.
36 Z. Hou, R. Chai, M. Zhang, C. Zhang, P. Chong, Z. Xu, G. Li and J. Lin, *Langmuir*, 2009, **25**, 12340–12348.
37 P. R. Jubu, F. K. Yam, V. M. Igba and K. P. Beh, *J. Solid State Chem.*, 2020, **290**, 121576.
38 Y. Zhang, N. A. W. Holzwarth and R. T. Williams, *Phys. Rev. B: Condens. Matter Mater. Phys.*, 1998, **57**, 12738–12750.
39 A. J. Kenyon, *Curr. Opin. Solid State Mater. Sci.*, 2003, **7**, 143–149.
40 J. Y. Jung, J. Y. Park, W. T. Hong, J. S. Joo, W. K. Jung and H. K. Yang, *J. Sci.:Adv. Mater. Devices*, 2024, **9**, 100710.
41 V. R. Kharabe, A. H. Oza and S. J. Dhoble, *Luminescence*, 2015, **30**, 432–438.
42 S. Murakami, M. Herren, D. Rau and M. Morita, *Inorg. Chim. Acta*, 2000, **300**, 1014–1021.
43 G. Jia, Y. Song, M. Yang, Y. Huang, L. Zhang and H. You, *Opt. Mater.*, 2009, **31**, 1032–1037.
44 S. K. Gupta, P. S. Ghosh, K. Sudarshan, R. Gupta, P. K. Pujari and R. M. Kadam, *Dalton Trans.*, 2015, **44**, 19097–19110.
45 Y. H. Kim, P. Arunkumar, B. Y. Kim, S. Unithrattil, E. Kim, S.-H. Moon, J. Y. Hyun, K. H. Kim, D. Lee, J.-S. Lee and W. B. Im, *Nat. Mater.*, 2017, **16**, 543–550.
46 X. Chen and Q. Meng, *J. Lumin.*, 2024, **275**, 120820.
47 R. Al-Gaashani, S. Radiman, A. R. Daud, N. Tabet and Y. Al-Douri, *Ceram. Int.*, 2013, **39**, 2283–2292.
48 Y. Zhou, J. Chen, O. M. Bakr and O. F. Mohammed, *ACS Energy Lett.*, 2021, **6**, 739–768.
49 L. Sudheendra, G. K. Das, C. Li, D. Stark, J. Cena, S. Cherry and I. M. Kennedy, *Chem. Mater.*, 2014, **26**, 1881–1888.
50 J. Ma, W. Zhu, L. Lei, D. Deng, Y. Hua, Y. M. Yang, S. Xu and P. N. Prasad, *ACS Appl. Mater. Interfaces*, 2021, **13**, 44596–44603.

